High-Performance Pyroelectric Generators Based on Mn-Doped Ferroelectric Single Crystals for Thermal Energy Harvesting

Zhan Peng[1], **Ting Zhang**[1]

Received February 1, 2026
Accepted May 18, 2026
Electronic access June 30, 2026

Addressing the growing demand for energy-efficient and self-powered systems, we fabricated pyroelectric generators (PEGs) based on the Mn-doped $Pb(In_{1/2}Nb_{1/2})O_3$-$Pb(Mg_{1/3}Nb_{2/3})O_3$-$PbTiO_3$ (Mn-PIMNT) ferroelectric single crystals with high pyroelectric properties to convert thermal energy from environment into electricity. The purpose of this work was to develop PEGs with high current and voltage outputs for powering low-power electronics or charging storage capacitors. Through optimized thermal annealing and electric-field poling treatments, the [111]-oriented Mn-PIMNT single crystals exhibited a large pyroelectric coefficient of $(8 \pm 0.4) \times 10^{-4}$ $C\,m^{-2}\,K^{-1}$ and suppression of relative dielectric permittivity of 488 $\pm$ 2, yielding a high figure of merit for pyroelectric energy conversion of 148 $\pm$ 16 J m^{-3} K^{-2} at room temperature, as well as high thermal stability up to 80 °C. The Mn-PIMNT (3.75 $cm^2 \times 0.04$ cm) based PEGs generated a large peak current of 2.4 $\pm$ 0.3 μA and a peak voltage of 5 $\pm$ 1 V measured after a full-wave bridge rectifier under thermal cycles with $\Delta T = 5.5 \pm 0.5$ °C and $\left(\frac{dT}{dt}\right)_{max} = 1.5 \pm 0.5$ °C s^{-1}. Furthermore, the PEG successfully illuminated a yellow LED, and charged storage capacitors, storing up to 60.5 μJ in a 100 μF capacitor within 2000 seconds. These results demonstrated the high-performance PEGs based on the Mn-PIMNT crystals with superior pyroelectric properties have promising for powering ultra-low-power electronics and wireless sensors.

Keywords: Ferroelectric Materials, Pyroelectric Generators, Thermal Energy Harvesting

Introduction

Energy harvesting systems can convert ambient energy into electrical energy, offering a pathway to supply sustainable green energy for self-powered sensors and systems such as wireless sensor networks and internet of things devices[1–4]. These technologies are attractive because they not only can eliminate the maintenance difficulties in replacement and environmental contamination compared to power supply by conventional batteries, but also can provide remote power supply for wireless networks in areas that are either inhospitable or difficult to reach[4–6].

There are a variety of energy harvesting approaches to harvest mechanical, solar and thermal energies from the environment to generate electrical energy[2–4]. The physical mechanisms of the energy generators are based on electromagnetic induction, piezoelectric, triboelectric, photovoltaic, thermoelectric, and pyroelectric effects, or coupled effects[2]. Each of these approaches offers unique advantages depending on the different environmental energy sources and specific applications[2–4]. The pyroelectric generators (PEGs) based on the pyroelectric effect can convert heat from the Sun, the Earth's interior, exhaust gases, resistance, human body, and so on, into electrical energy[7–10]. The pyroelectric energy harvesters can offer high output performance and rapid response, as well as high reliability and environmental adaptability, making them potential for powering ultra-low-power electronic devices, e.g., wireless sensor nodes, wearable electronics, structure-embedded micro-sensors and medical implants[11–14]. Unlike thermoelectrics that convert a spatial temperature gradient into electrical energy via the Seebeck effect, pyroelectrics only require a temporal variation in temperature to realize energy conversion, making pyroelectrics highly desirable in environments where the temperature gradients are difficult to establish[2].

The pyroelectric effect describes the temperature-dependent evolution of spontaneous polarization (P), resulting in changes in the surface charge density of the pyroelectrics[7]. Based on thermal–electrical cycles, researchers were established a dimensionless figure of merit (FOM) for pyroelectric energy conversion, quantified through parameters by $F_E = p^2/(\varepsilon_0 \varepsilon_r)$[10], where ε_0 is permittivity of free space, and p and ε_r are the pyroelectric coefficient and the relative dielectric permittivity along the poling direction, respectively. Therefore, a high-performance pyroelectric energy conversion material should have both a high p and a low ε_r. $Pb(Mg_{1/3}Nb_{2/3})O_3$-$PbTiO_3$ (PMNT) ferroelectric single crystals oriented along their polar axis were reported to show both a high p and a low ε_r compared with that oriented

[1] *Shanghai World Foreign Language Academy, Shanghai, China*

along their nonpolar axis [15].

Compared to these binary counterparts, the [111]-oriented rhombohedral $Pb(In_{1/2}Nb_{1/2})O_3$ – $Pb(Mg_{1/3}Nb_{2/3})O_3$ – $PbTiO_3$ (PIMNT) ternary single crystals were reported to exhibit not only high figures of merit, but also better thermal stability and wider operation temperature range due to their higher Curie temperature [16,17]. Further investigations have demonstrated that the pyroelectric properties of the single crystals could be improved by Mn-doping [18,19]. Based on crystal chemical coordination principles, Mn ions preferentially substituted Ti^{4+}, and oxygen vacancies (V_O) produced, forming a defect dipole Mn_{Ti}-V_O. The domain walls of the single crystals were pinned by the dopant dipolar defects, which enhanced the pyroelectric properties and suppressed the dielectric properties [18,19]. Though pyroelectric properties of the ferroelectric single crystals were extensively studied for infrared detection applications [15–19], systematic investigations on the [111]-oriented Mn-doped PIMNT rhombohedral single crystals based pyroelectric generators under realistic contact thermal excitation for thermal energy harvesting remains limited. We hypothesize that for rhombohedral PIMNT single crystals with high Curie temperature, the synergistic strategy of Mn-doping, [111] crystallographic orientation, and poling along this polar axis will effectively enhance the pyroelectric coefficient and reduce the dielectric permittivity, thereby maximizing the figure of merit ($F_E = p^2/(\varepsilon_0\varepsilon_r)$) and ultimately leading to superior output performance in pyroelectric energy harvesters.

The output performance of PEGs not only depends on the pyroelectric properties of materials, but also relates to the thermodynamic cycles and device structures for pyroelectric energy conversion [7–10]. S. Pandya, et al. reported that implementation of solid-state pyroelectric Ericsson cycles based on the PMN–0.32PT thin films with enhanced properties induced by high electric field, yielded a maximum energy density and power density of 1.06 J cm^{-3} and 526 W cm^{-3} per cycle, respectively, with temperature fluctuation ΔT of 60 – 80 °C. This work suggested that pyroelectric energy conversion could potentially compete with thermoelectrics, in particular, for energy harvesting from low-grade waste heat [13].

In this work, we fabricated PEGs using 0.5mol% Mn-doped $0.15Pb(In_{1/2}Nb_{1/2})O_3$-$0.55Pb(Mg_{1/3}Nb_{2/3})O_3$-$0.30PbTiO_3$ (Mn-PIMNT) with high pyroelectric properties for thermal energy harvesting. The work aimed to develop PEGs with high current and voltage outputs for powering low-power electronics or charging storage capacitors. Through optimized thermal annealing and electric-field poling treatments, our results consistently showed that the [111]-oriented Mn-PIMNT rhombohedral single crystals exhibited large pyroelectric coefficients and suppression of dielectric permittivity, yielding high figure of merit (F_E), as well as thermal stability up to 80 °C. The Mn-PIMNT (3.75 $cm^2 \times 0.04$ cm) based PEG successfully illuminated a yellow LED and charged storage capacitors. These results demonstrated that the PEGs based on the Mn-PIMNT crystals with superior pyroelectric properties had significant potential for powering ultra-low-power electronics and wireless sensors.

Methods

Preparation of single-crystal specimen

0.5mol% Mn-doped $0.15Pb(In_{1/2}Nb_{1/2})O_3$ – $0.55Pb(Mg_{1/3}Nb_{2/3})O_3$ – $0.30PbTiO_3$ single crystals (abbreviated as Mn-PIMNT) were grown using a modified Bridgman technique by Shanghai Institute of Ceramics, Chinese Academy of Sciences [20]. The crystals were oriented along the [111] direction using X-ray diffraction, and then cut into thin slices. These slices were mechanically thinned and polished to a final thickness of 400 ± 1 μm with surface roughness $R_a < 10$ nm by a Precision Polishing System (MULTIPREP™ 12", Allied High Tech Products, Inc., USA) to achieve parallel and perfect surfaces (Figure 1(b)). To relieve internal stresses, the polished slices were annealed in a Muffle furnace (KSL-1200X, Hefei Kejing Material Technology Co., Ltd., China). The above thermal treatment was performed in ambient atmosphere, heating to 600 °C at a rate of 1 °C min^{-1}, holding for 1 hour, then cooling naturally to room temperature in ambient atmosphere.

Fabrication of PEGs based on Mn-PIMNT single crystals

The PEG consisted of a Mn-PIMNT single-crystal slice sandwiched between two gold (Au) electrodes (Figure 1(b)). Au electrodes with excellent conductivity were deposited on both polished [111] surfaces of the Mn-PIMNT slice using a Vacuum Magnetron Sputtering System (JS-1600, Beijing HTCY Technology Co., Ltd., China). The Au/Mn-PIMNT/Au was then poled under a DC electric field of 10 kV cm^{-1} in silicone oil at room temperature for 15 min to align the ferroelectric domains using a Programmable Withstanding Voltage Tester (CS9912BN, Changzhou Cangsheng Electronic Co., Ltd., China). The poling conditions were chosen based on the saturation behavior observed in the polarization-electric field (*P-E*) hysteresis loops at room temperature, where the polarization saturated enough under electric field near 10 kV cm^{-1}, which was commonly used for the ferroelectric single crystals [21].

Structure and electrical characterization of Mn-PIMNT single crystals

The crystallographic structure and orientation were examined at room temperature using an X-ray diffraction (XRD) spec-

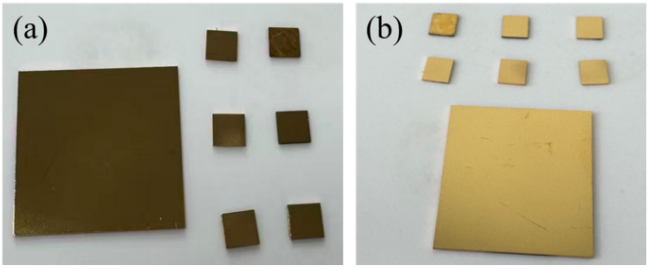

Fig. 1 The photographs of (a) the polished Mn-PIMNT single-crystal specimen after thermal annealing and (b) single-crystal slices sandwiched between gold (Au) electrodes.

trometer with Cu K_α radiation (Bruker D8 Advance Diffractometer, Germany). The polarization-electric field (P – E) hysteresis loops and current-electric field (I – E) loops were measured at room temperature at 10 Hz using a ferroelectric test system (TF analyzer 2000, aixACCT, Germany). The temperature-dependent pyroelectric coefficient $p(T)$ was measured by the Byer-Roundy method[22], using a pyroelectric coefficient test system (ZR-1, PCTS-2000, Huzhong University of Science and Technology, China), which was determined from the measured pyroelectric current (i_p) using a Keithley 617 electrometer, and the heating rate (dT/dt), as well as the effective area (A) normal to the [111] direction, as described by $p(T) = i_p/A(dT/dt)$. The temperature increased linearly with time from room temperature to 250 °C with dT/dt = 1 °C /min. The temperature/frequency-dependent dielectric permittivity (ε_r) and loss tangent ($\tan\delta$) over the temperature range (room temperature to 250 °C) and the frequency range (40 – 2000 Hz) were measured by an impedance analyzer (DMS2000, Agilent 4294A, Agilent Technologies Inc., America). DC resistance was measured by a semiconductor characterization system (Keithley 4200 SCS, Tektronix, Inc., USA) with a high-impedance ($> 10^{12}$ Ω). All measurements were performed on 6 samples with 3 trials per sample, and values represented mean ± standard deviation.

The output performance characterization of the PEGs

To investigate the output performance of the PEGs based on Mn-PIMNT single crystals under periodic thermal cycling, a series of measurements was conducted. The schematic diagram of the experimental setup for simultaneously measuring temperature by a thermometer, and current by an ammeter or voltage by a voltmeter was shown in Figure 2. A PEG (Au/Mn-PIMNT/Au) was fixed on a glass plate, and a K-type thermocouple digital thermometer (YET-610L, Shenzhen Yu Wen Jing Gong Technology Co., Ltd.) was mounted between the PEG and glass plate to measure PEG's temperature. Thermal cycles ($\Delta T = 5.5 \pm 0.5$ °C, period $\tau = 20$ s) were induced through alternating exposure to heated and cooled sources for equal time. Electrical contacts were made by adhering copper wires to the Au electrodes with conductive copper tape, then connected to the current or voltage measurement system. To convert AC generated by the PEG to DC, the PEG was connected to a full-wave bridge rectifier configuration comprising 4 Germanium diodes (1N60P) with ultra-low leakage current. In response to the periodically varying temperature, the generated pyroelectric current was measured by a semiconductor characterization system (Keithley 4200 SCS, Tektronix, Inc., USA) with an input impedance higher than 10^{12} Ω and a bandwidth up to 5 MHz, and the output voltage was measured by a voltmeter (UT61B+, UNI-Trend Technology Co., Ltd., China) with an input resistance of 10 MΩ and a bandwidth of 40 – 500 Hz, which was not an intrinsic open-circuit device voltage. The current and voltage were measured after the rectifier bridge.

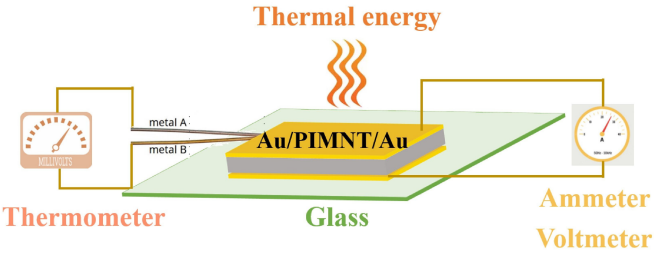

Fig. 2 The schematic diagram of the experimental setup for temperature, current or voltage measurements of the PEGs (Au/PIMNT/Au).

Results

The structures and electrical properties of Mn-PIMNT single crystals

The structures and electrical properties of [111]-oriented Mn-PIMNT single crystals were shown in Figure 3. The room-temperature X-ray diffraction (XRD) pattern as shown in Figure 3(a) revealed that the as-grown Mn-PIMNT single crystals exhibited a pure ABO_3-type perovskite structure and excellent crystal quality. The (111) diffraction peak splitting at 38.391° and 38.482° (inset of Figure 3(a)) was a fingerprint of rhombohedral symmetry (R3m) in Mn-PIMNT, caused by polarization-driven anisotropic lattice distortion along the <111> direction[23]. Polarization–electric field (P–E) hysteresis loops and current-electric field (I–E) loops of the Mn-PIMNT single crystals were shown in Figure 3(b). The polarization of the Mn-PIMNT saturated as the applied electric field escalated to 8 kV cm^{-1} and then increased linearly with E increasing to 10 kV cm^{-1}. The average remnant polarization (P_r) and coercive field (E_C) were 42.4 μC cm^{-2}

and 6.7 kV cm^{-1} at room temperature, respectively. The remnant polarization showed a negative offset of about -1.8 μC cm^{-2}, while E_C showed a positive offset of 1 kV cm^{-1}, which was attributed to the Mn_{Ti}-V_O dipole defects pinning domain walls [18,19]. Two current peaks in the *I–E* curve at E_C were due to the ferroelectric domain switching. Figures 3(c) and 3(d) showed the temperature-dependent pyroelectric coefficient (p) from room temperature (RT) to 250 °C and the temperature/frequency-dependent dielectric permittivity (ε_r) and dielectric loss (tan δ) over the temperature range (RT to 250 °C) and frequency range (40 – 2000 Hz) for the single crystals. From the test results, the pyroelectric coefficient of the crystals was $(8 \pm 0.4) \times 10^{-4}$ C m^{-2} K^{-1} at room temperature, and increased nearly linearly with temperature increasing up to 80 °C (Figure 3(c)). Through literature searches, the two peaks around 127 °C and 156 °C in the *p-T* curve, corresponded to the rhombohedral to tetragonal, and tetragonal to cubic phase transitions, respectively [16–18]. The values of ε_r and tanδ were 488 ± 2 and 0.001 ± 0.0003 at room temperature and 100 Hz, respectively, and showed nearly frequency independence over the experimental frequency range (Inset of Figure 3(d)). At 1 kHz, the values of ε_r and tanδ increased linearly up to 80 °C, followed by a dielectric anomaly around 133 °C and the maxima at 156 °C (Figure 3(d)), corresponding to the rhombohedral to tetragonal, and tetragonal to cubic phase transitions [16, 17,18], consistent with the phase transition temperatures as shown in *p-T* curve. The pyroelectric and dielectric properties of those specimen were very similar and stable. These findings showed that the Mn-PIMNT single crystals exhibited both excellent pyroelectric properties and thermal stability over the environmental temperature range for thermal energy harvesting applications.

Output performance of the PEGs based on the Mn-PIMNT single crystals

The equivalent circuit of a PEG can be modelled as a current source in parallel with a capacitance (C_P) and a resistance (R_P) [7]. The PEGs generated alternating current (AC) when heating and cooling, which should be converted to a direct current (DC) or specific electrical pulses for powering the electronic devices. The equivalent circuit diagrams of a PEG connected to the full-wave bridge rectifier circuit for measuring current, voltage, and progressive voltage buildup across a loading capacitor (C_L) during charging by the PEG were shown in Figure 4.

Based on the thermal–electrical cycles, the pyroelectric current $\left(\mathrm{I}_p = \frac{\mathrm{d}Q}{\mathrm{d}t} = p\mathrm{A}\frac{\mathrm{d}T}{\mathrm{d}t}\right)$, voltage $\left(\mathrm{V_{OC}} = \frac{\mathrm{Q}}{\mathrm{C}} = \frac{\mathrm{pd}\Delta T}{\varepsilon_0\varepsilon_r}\right)$ and energy storage $\mathrm{E} = \frac{1}{2}\mathrm{CV_{OC}^2} = \frac{1}{2}\frac{p^2\mathrm{A}d(\Delta T)^2}{\varepsilon_0\varepsilon_r}$ of a PEG depended on not only the pyroelectric coefficient (p) and dielectric permittivity (ε_r) of a pyroelectric material, but also the effective area (A), thickness (d), and temperature fluctuation (ΔT and $\mathrm{d}T/\mathrm{d}t$) of a PEG [7,10], where Q and C were the net charge and capacitance of a PEG, respectively. The values of p and ε_r of the Mn-PIMNT were nearly constant near room temperature (Figures 3(c) and 3(d)). Increment of the effective area A, temperature variation (ΔT) and temperature-change rate ($\mathrm{d}T/\mathrm{d}t$) was an effective way to enhance the output performance of PEGs. Therefore, we used a warm hand to heat and a cold water bag to cool the Mn-PIMNT $(3.75\ \mathrm{cm}^2 \times 0.04\ \mathrm{cm})$ based PEG to obtain a ΔT of 5 – 6 K per thermal cycle with period τ = 20 s (Figure 5(a)) to generate large output current and voltage. The manual method to induce thermal cycles was chosen to simulate real-world application conditions, which would introduce some operational variability. Therefore, the generated current and voltage and their corresponding temperature with time were measured over 12 complete thermal cycles including 4 consecutive cycles per run and 3 independent repeated runs. The values of temperature change, peak current, and peak voltage represented the mean ± standard deviation determined from multiple cycles. The temperature increased suddenly when heating, and decreased sharply when cooling for all thermodynamic cycles (Figure 5(a)). The corresponding temperature-change rate $(\mathrm{d}T/\mathrm{d}t)$ was obtained by taking a derivative with respect to the measured temperature of PEGs. In response to the periodically varying temperature, the output current of the PEG measured after the rectifier bridge increased as $\mathrm{d}T/\mathrm{d}t$ increased, reached up to 2.4 ± 0.3 μA as $\mathrm{d}T/\mathrm{d}t$ reached the highest point (1.5 ± 0.5 °C s^{-1}), gradually decreased as $\mathrm{d}T/\mathrm{d}t$ decreased, and disappeared when $\mathrm{d}T/\mathrm{d}t$ decreased to zero (Figure 5(b)). The decay time of output current [7] by defining the time from 100% to 37% (1/e) of its peak value was about 1.0 s on heating and 1.8 s on cooling. These values represented effective thermal time constants for the respective halves of the cycle. The asymmetry of the generated current signal was due to $(\mathrm{d}T/\mathrm{d}t)_{\max}$ on heating being higher than on cooling, owing to the asymmetrical heat transmission between the heating process from T_0 to $T_0 + \Delta T$ and the cooling process from $T_0 + \Delta T$ to T. To quantitatively link this asymmetry to the material properties and device geometry, the time constant was estimated using the thermal properties of the [001] oriented Mn-doped tetragonal PIMNT single crystals with volume specific heat (C_V) of 2.5×10^6 J m^{-3} K^{-1} and thermal diffusivity (D) of 4.4×10^{-7} m^2 s^{-1} [19]. For one-dimensional heat diffusion across the PEG thickness (L = 0.04 cm), the intrinsic thermal diffusion time ($\tau_{\mathrm{diff}} = L^2/D$) was about 0.36 s, which was shorter than the measured decay times (1.0 s and 1.8 s), indicating that the thermal response was not limited by internal heat diffusion within the crystal, rather dominated by the external thermal resistance (R_{th}) at the PEG and environment interface (hand/water bag) [24]. The effective time constant was determined by $\tau_{\mathrm{diff}} = R_{th} \cdot C_{th}$, where C_{th} was the PEG's heat capacity [25]. The observed asymmetry (τ_c

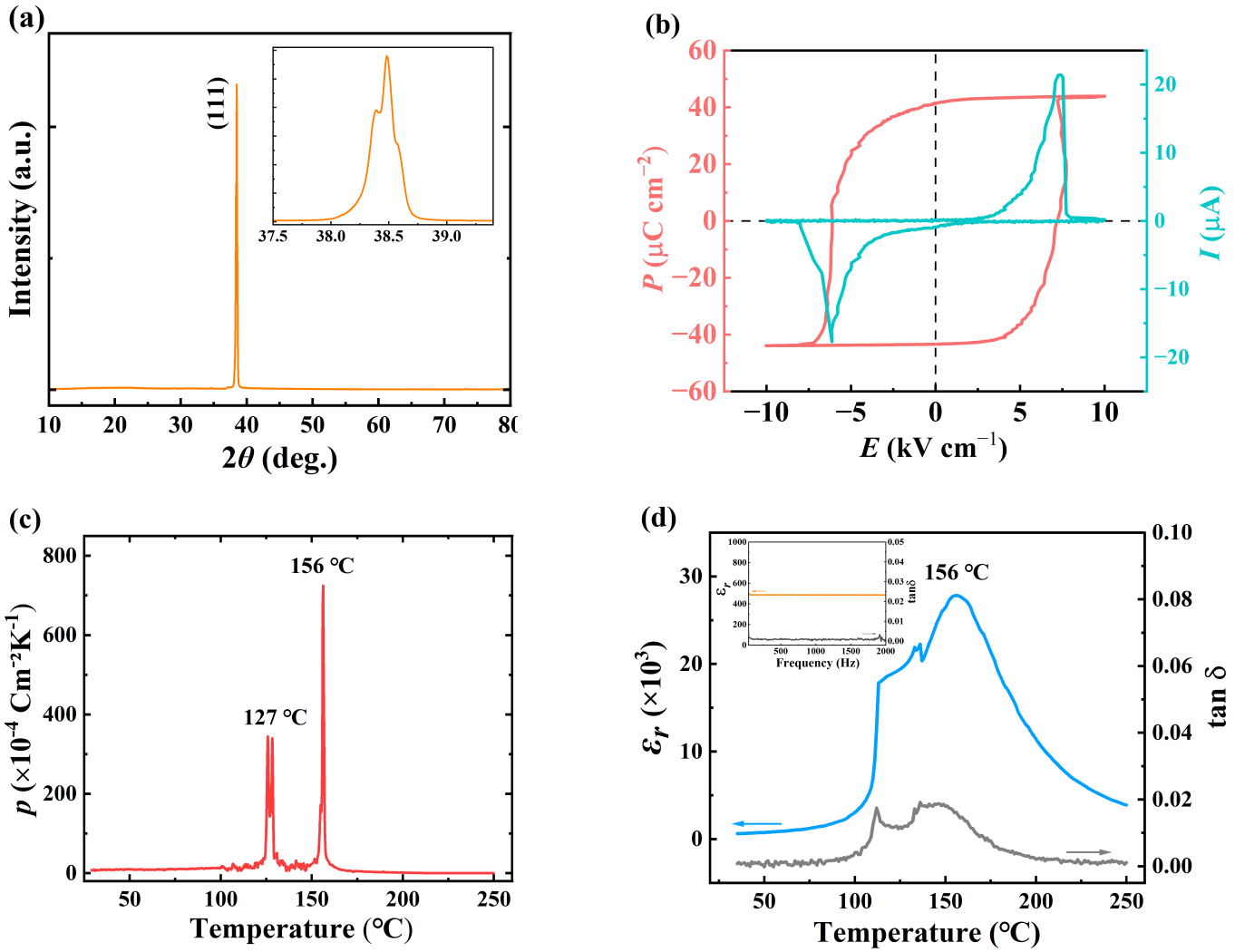

Fig. 3 The structures and electrical properties of [111]-oriented Mn-PIMNT single crystals. (a) Wide angle θ-2θ scans XRD pattern at room temperature. The inset was enlargement of XRD pattern around diffraction peaks. (b) Polarization–electric field (P–E) hysteresis loops and current-electric field (I–E) loops measured at room temperature and 10 Hz. (c) The pyroelectric coefficient (p) as a function of temperature of the poled crystals. (d) The dielectric permittivity (ε_r) and loss tangent (tanδ) as a function of temperature at 1 kHz, and as a function of frequency at room temperature (inset of d) of the poled crystals.

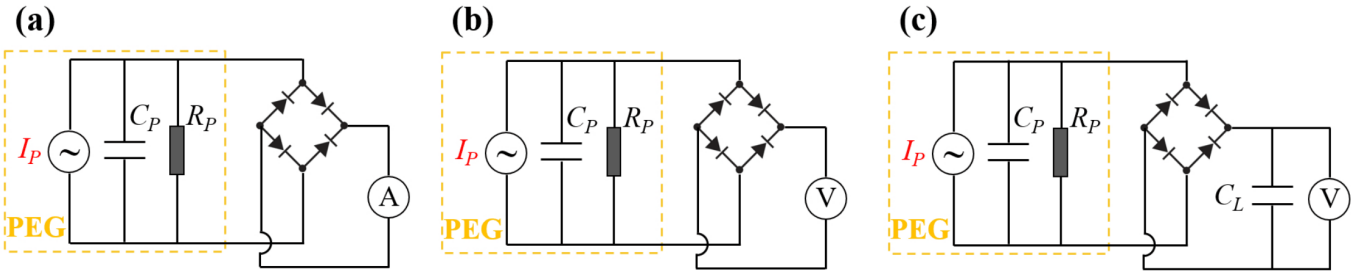

Fig. 4 The equivalent circuit diagram of a PEG connected to a full-wave bridge rectifier circuit for measuring (a) current, (b) voltage, and (c) progressive voltage buildup across a loading capacitor (C_L) during charging by the PEG.

$> \tau_h$) directly quantified that the effective thermal resistance during cooling was larger than during heating, consistent with the less efficient heat transfer to the water bag compared to the hand contact[24]. In addition, the PEGs exhibited high peak voltages of about 5 ± 1 V for thermal cycles with ΔT = 5.5 ± 0.5 °C (Figure 5(c)). Despite the observed variability introduced by the manual cycling technique, the measured output current and voltage consistently corresponded to the temperature change by the thermal stimulus in every cycle and remained consistent across repeated cycles as shown in Figure 5, which demonstrated its functional viability and reproducible performance under these dynamic, application-relevant conditions.

To confirm the efficient charging capability of the PEGs, the PEG was connected an energy storage capacitor (C_L) through a full-wave bridge rectifier configuration (Figure 4(c)). The rectified energy was stored in a C_L, and progressive voltage buildup across the different energy storage capacitors during charging by the PEGs as shown in Figure 6. The non-smooth charging curves over many cycles were mainly caused by the manual thermal cycling method (warm hand and cold water bag), which inherently introduced variability, but could simulate the irregular thermal fluctuations found in real-world environments such as body heat and ambient temperature changes. In addition, the finite input impedance of the voltmeter (R_V = 10 MΩ), in parallel with the storage capacitor, formed a discharge path with a time constant $\tau = R_L C_L$. This finite time constant meant that the loading capacitor was simultaneously charged by the PEG and slowly discharged through the voltmeter during the voltage measurement. Therefore, the observed step-like or non-monotonic voltage incensement was a superposition of the intermittent charging pulses from the PEG and the continuous slow discharge through the voltmeter. The maximum attainable voltage (U_{max}) reached 2.8 V, 1.8 V, 1.0 V and 1.1 V for C_L of 4.7 μF, 10 μF, 47 μF and 100 μF, respectively (Figure 6). As the value of C_L increased, the values of U_{max} across the energy storage capacitor decreased, while the values of energy (E) stored in the capacitors increased. The total energy storage in the capacitor with C_L = 100 μF reached 60.5 μJ after 2000 s, despite a slower voltage rise with time. These findings showed that the PEGs based on the Mn-PIMNT single crystals with high pyroelectric properties (Figure 3) showed high output performance (Figure 6).

Discussion

From the test results, large pyroelectric coefficient and low dielectric permittivity were achieved for the [111]-oriented rhombohedral Mn-PIMNT single crystals through selecting appropriate composition and orientation, optimizing thermal annealing and electric-field poling treatments (Figure 3). The room-temperature pyroelectric properties of the Mn-doped PIMNT single crystals were summarized in Table 1 and the pyroelectric properties of pure PIMNT single crystals were list for comparison. The pyroelectric coefficient of Mn-PIMNT single crystals was larger than that of pure PIMNT single crystals[16]. Furthermore, the dielectric permittivity was also suppressed by Mn-doping. The combination of enhanced pyroelectric coefficient and suppressed dielectric permittivity resulted in an enhancement of figure of merit (F_E) of 148 ± 16 J m^{-3} K^{-2} for the [111]-oriented rhombohedral Mn-PIMNT single crystals compared to the undoped counterparts (120 J m^{-3} K^{-2})[16]. The pyroelectric coefficient and dielectric permittivity remained unchanged at operating temperatures in ambient, well below the Curie temperature (T_C), which ensured the working reliability and repetitions in every energy conversion even seasonal changes. The large pyroelectric properties with high thermal stability up to 80 °C made the Mn-PIMNT single crystals promising for pyroelectric energy conversion. It should be noted that the structures, pyroelectric properties and thermal stability of this kind of single crystals were dependent on their composition and orientation[15–19]. Therefore, we should select the appropriate single-crystal compositions for thermal energy harvesting according to both the operating environment and the performance requirement.

The Mn-PIMNT single crystals based PEGs exhibited a large peak current of 2.4 ± 0.3 μA after rectification, corresponding to the maximum dT/dt of 1.5 ± 0.5 °C s^{-1} as shown in Figures 5(a) and 5(b)). The generated current of the PEG was much higher than the expected value based on the measured pyroelectric coefficients under constant strain, quasi-static and uniform heating conditions, indicating an enhanced effective pyroelectric response under device operational conditions. As all ferroelectric crystals are also piezoelectric, the thermal expansion induced by temperature change leads to a strain which operates through the piezoelectric effect to give an additional secondary pyroelectric effect[22,25]. In addition, when a temperature gradient exists in ferroelectrics to set up internal stress gradients, which can produce polarization via the piezoelectric effect, contributing a tertiary pyroelectric response[22]. Consequently, the enhanced current generated by the PEG under unclamped, rapid and non-uniform thermal cycling conditions should be attributed to the secondary and tertiary pyroelectric response superimposed on the primary pyroelectric response, which should be described by $I_{total} = I_{primary} + I_{secondary} + I_{tertiary}$[22]. The output current of the PEG based on the Mn-PIMNT single crystals was notably higher than the current (I = – 4.5 nA) reported for the PEG based on $Pb(Zr_xTi_{1-x})O_3$ (PZT) ceramics, even though the latter device utilized a larger area (49 × 49 mm^2) and larger temperature fluctuation (ΔT = 8 K and dT/dt = 7.6 K/s)[10], which suggested a substantially higher output current per unit area per unit dT/dt for the PEG based on the Mn-

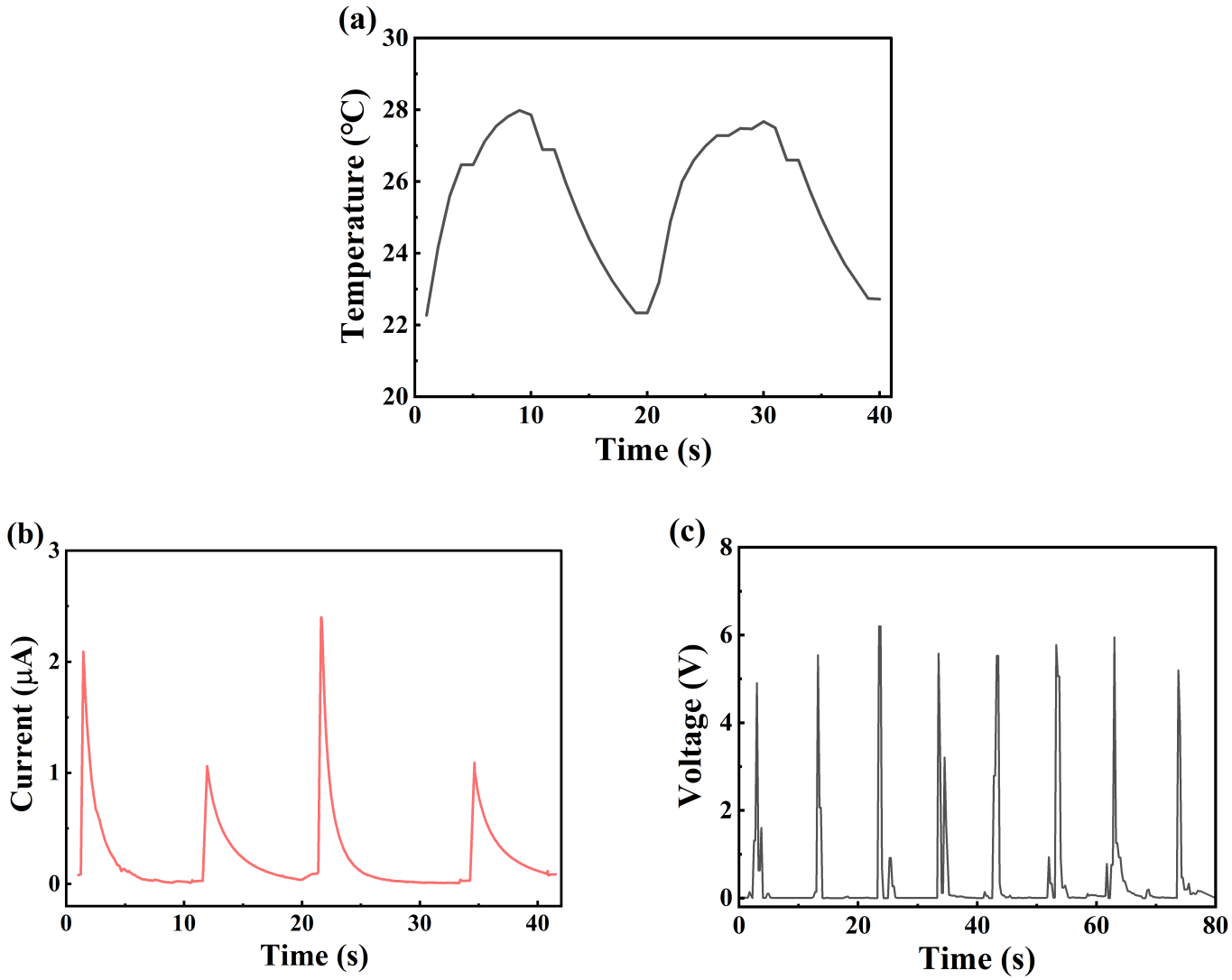

Fig. 5 The output current and voltage of the PEGs based on Mn-PIMNT ($3.75\ cm^2 \times 0.04\ cm$) measured after the full-wave bridge rectifier for $\Delta T = 5.5 \pm 0.5\ ^\circ C$ and thermodynamic cycle $\tau = 20$ s. (a) The measured temperature by periodically heating using a warm hand and cooling by a cold water bag. (b) The output current of the PEGs. (c) The output voltage of the PEGs measured by a voltmeter with $R_V = 10\ M\Omega$.

Table 1 Pyroelectric properties of the [111]-oriented rhombohedral Mn-doped PIMNT single crystals at room temperature, and the [111]-oriented rhombohedral pure PIMNT single crystals list for comparison [16].

	T_C (°C)	p (10^{-4} C m^{-2} K^{-1})	ε_r (100 Hz)	$\tan\delta$ (100 Hz)	F_E (J m^{-3} K^{-2})	Refs.
Mn-PIMNT	156	8 ± 0.4	488 ± 2	0.001 ± 0.0003	148 ± 16	This work
PIMNT	180	7.5	529	0.001	120	16

PIMNT single crystals. The higher output current for the PEG based on the Mn-PIMNT was attributed to the higher pyroelectric properties of the single crystals compared to the conventional PZT ceramics [26], highlighting the advantage of Mn-PIMNT for high-performance thermal energy harvesting. Furthermore, the output peak voltage (5 ± 1 V) of the PEG

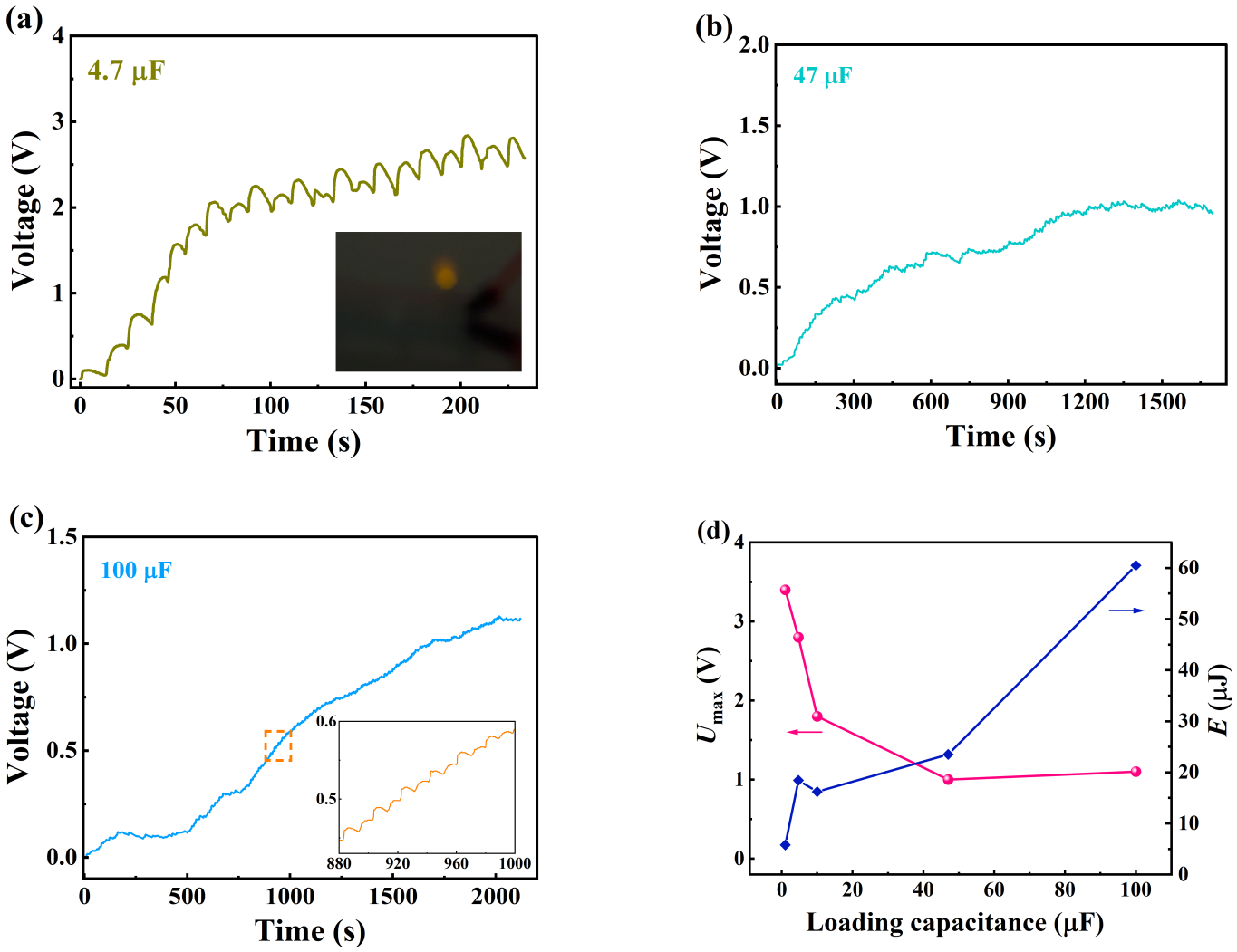

Fig. 6 Progressive voltage buildup across the energy storage capacitors during charging by the PEG based on Mn-PIMNT ($3.75\ cm^2 \times 0.04$ cm) measured after the full-wave bridge rectifier circuit by a voltmeter with resistance of 10 MΩ. The voltage (U) on the energy storage capacitor (C_L) for (a) C_L = 4.7 μF, (b) C_L = 47 μF, and (c) C_L = 100 μF during charging by the PEG. The inset of (c) displayed the enlarged view of the area marked by a rectangle (orange). (d) The measured maximum voltage (U_{max}) on the capacitors and corresponding energy stored in the capacitors.

(Figure 5(c)) was much higher than that of the PEG based on PVDF films with output voltage of 1.2 V under a higher input impedance of 100 MΩ and a much larger temperature fluctuation (ΔT = 47 K, dT/dt = 25 K/s)[27].

Since the output voltage was highly dependent on voltmeter's resistance, the peak voltage recorded by a voltmeter with a resistance of 10 MΩ was much lower than the theoretical value of open-circuit voltage[27]. This substantial discrepancy raised from the voltage-divider effect between the voltmeter's internal resistance (R_V) and the PEG's inherent resistance (R_P)[27]. Low-impedance voltmeters (R_V = 10 MΩ $\ll$ R_P = 30 GΩ) created parallel current leakage paths, artificially suppressing the measured voltage. The ideal conditions for the voltmeter to get the intrinsic voltage are $R_V \to \infty$ (or $R_V \gg R_P$) and $C_V \to 0$ (or $C_V \ll C_P$), which might be impractical for many cases[27]. The high output current and voltage suggested that the Mn-PIMNT single crystals possessed excellent pyroelectric properties over the environmental temperature range, leading to high-performance PEGs for harvesting thermal energy in ambient (Figure 5). Since the magnitude and waveform of the output current and voltage of the PEGs were determined by dT/dt and ΔT respectively[7,10], further performance enhancements for the PEGs could be realized by increasing temperature fluctuation (dT/dt and ΔT) and PEG's

effective area or developing multilayer PEGs.

The generated electrical energy was stored in energy storage capacitors (C_L), and progressive voltage buildup across C_L during charging by the PEGs (Figure 6(a-c)). The maximum attainable voltage (U_{max}) decreased from 2.8 V to 1.1 V with increasing loading capacitance (C_L) from 4.7 to 100 μF. The voltage on the capacitors remained below the output voltage of the PEG, creating sustained charge transfer potential. For a lower C_L, such as C_L = 4.7 μF (Figure 6(a)), the voltage ($U = Q/C_L$) was larger with less charge transfer (Q) than that of the larger C_L. The generated electrical energy of the PEG could drive a yellow, red, or green light emitting diode (LED) connected to the capacitor with C_L = 4.7 μF (inset of Figure 6(a)). However, lower C_L systems suffered from rapid charge dissipation through loads, yielding a reduced time constant $\tau = R_L C_L$. Larger capacitors with C_L of 47 μF and 100 μF exhibited a voltage of about 1 V by charging for a longer time (Figure 6(b-c)). For the capacitor with C_L = 100 μF, the average charge transferred per cycle was 1.1± 0.1 μC for 100 thermal cycles (Figure 6(c)). During 880 – 1200 s, the capacitor achieved a voltage increment from 0.447 to 0.590 V after 6 thermal cycles, with a corresponding average charge rate of 2.4 ± 0.1 μC per cycle (inset of Figure 6(c)). As the loading capacitance increased, the value of U_{max} across the energy storage capacitors decreased, while the total energy ($E = \frac{1}{2} C_L U^2$) stored in the capacitors increased (Figure 6(d)). The total energy storage in the capacitor with C_L = 100 μF reached 60.5 μJ after 2000 s, despite a slower voltage rise with time. Optimal C_L selection should balance voltage and charging time for the target energy density. The analysis focused on the trends and average performance over many cycles to assess functional viability under such conditions. The results confirmed the efficient charging capability of the PEGs based on Mn-PIMNT single crystals that showed potential applications in low-power electronic devices.

To address the significant output fluctuation characteristics of pyroelectric generators, a pyroelectric energy harvesting system should be proposed to realize a stable power output. The system adopted a modular architecture of "pyroelectric generator + rectifier circuit + energy storage unit + voltage regulator" (Figure 7), enabling flexible configuration according to different application requirements. This modular design is expected to break through the technical bottleneck of instability and the inapplicability in existing pyroelectric energy harvesters. PEGs have highlighted the demand for battery-free, long-lasting, remote and low-power devices. Despite advances in the output current, voltage, energy and power densities, much needs to be done for practical applications.

High-performance pyroelectric generators (PEGs) were developed utilizing the Mn-PIMNT single crystals with large pyroelectric properties and high thermal stability for high-efficient pyroelectric energy conversion. The PEGs can convert thermal energy from the Sun, the Earth's interior, exhaust gases, resistance, human body, and so on, into electrical energy, which has significant potential for powering ultra-low-power electronic and wireless sensors in remote environments.

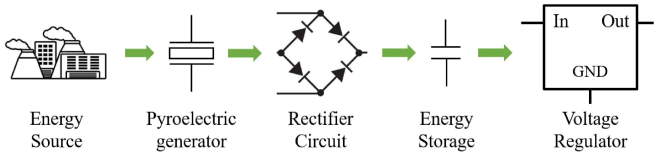

Fig. 7 The pyroelectric energy harvesting systems used to realize stable power output.

Conclusion

In summary, the pyroelectric generators (PEGs) have been fabricated for thermal energy harvesting utilizing the Mn-PIMNT single crystals with large pyroelectric properties ($p = (8 \pm 0.4) \times 10^{-4}$ C m^{-2} K^{-1} and F_E = 148 ± 16 J m^{-3} K^{-2}) and high thermal stability up to 80 °C. The Mn-PIMNT (3.75 cm^2 × 0.04 cm) based PEGs generated a large peak current of 2.4 ± 0.3 μA, and a peak voltage of 5 ± 1 V after rectification under thermal cycles with ΔT = 5.5 ± 0.5 °C and $(dT/dt)_{max}$ = 1.5 ± 0.5 °C s^{-1}. The maximum attainable voltage (U_{max}) across the energy storage capacitors charged by the PEG decreased from 2.8 V to 1.1 V with loading capacitance (C_L) increasing from 4.7 to 100 μF, which would be higher if measured by a voltmeter with higher impedance. The total energy ($E = \frac{1}{2} C_L U^2$) stored in the capacitors increased with C_L and charging time increasing, and increased to 60.5 μJ on C_L = 100 μF after 2000 s, which could power a typical wireless sensor node in a low-power sensing or standby state with an average power consumption on the order of 10 μW for about 6 seconds. The results demonstrated that the PEGs based on the Mn-PIMNT single crystals with high pyroelectric properties have significant potential for powering ultra-low-power electronics and wireless sensors.

Remaining Questions and Future Studies

The single-device configuration and output performance characterization under controlled laboratory conditions highlighted the potential applications of the PEGs for ultra-low-power devices. Despite these developments, issues such as scientific rigor and reproducibility of property characterization require thermal cycling apparatus with high-precision and real-time temperature control and measurements.

Beyond of measurement technique, the structural design, large output power and electric controllability of PEGs, and system integration to applications, remain the key challenges.

Future improvement or implementations should focus on developing multilayer PEGs or hybrid energy generators combined piezoelectric, photovoltaic and pyroelectric effects to harvest mechanical, solar, and thermal energies from the environment to enhance total output performance, and then dedicating power management circuits to rectify, regulate, and efficiently store the harvested energy, as well as developing system integration for real-world applications.

Acknowledgements

I hereby acknowledge all those who provided me with support and guidance to complete this research work, especially Professor Tiannan Yang from Shanghai Jiao Tong University.

References

1 Z. Wang, Self-powered nanosensors and nanosystems. Advanced Materials. Vol. 24, pg. 280–285 (2012). doi:10.1002/adma.201102958.

2 H. Ryu, H. Yoon, S. Kim, Hybrid energy harvesters: toward sustainable energy harvesting. Advanced Materials. Vol. 31, pg. 1802898 (2019). doi:10.1002/adma.201802898.

3 H. Liu, H. Fu, L. Sun, C. Lee, E. M. Yeatman, Hybrid energy harvesting technology: from materials, structural design, system integration to applications. Renewable and Sustainable Energy Reviews. Vol. 137, pg. 110473 (2021). doi:10.1016/j.rser.2020.110473.

4 M. T. Ansar, T. S. Tran, R. Raees, V. T. Dau, D. V. Dao, Piezo-pyro-phototronics: a propitious pathway for ultrasensitive sensing and self-power applications. Nano Energy. Vol. 138, pg. 110831 (2025). doi:10.1016/j.nanoen.2025.110831.

5 N. Golafshan, S. Patra, N. D. Huynh, N. Gadegaard, A. Boisen, Self-powered implantable and ingestible devices: harvesting energy within the body. Materials Today. Vol. 87, pg. 403–421 (2025). doi:10.1016/j.mattod.2025.05.006.

6 X. Cui, L. Wu, C. Zhang, Z. Li, Implantable self-powered systems for electrical stimulation medical devices. Advanced Science. Vol. 12, pg. 2412044 (2025). doi:10.1002/advs.202412044.

7 E. Fatuzzo, H. Kiess, R. Nitsche, Theoretical efficiency of pyroelectric power converters. Journal of Applied Physics. Vol. 37, pg. 510–516 (1966). doi:10.1063/1.1708205.

8 G. Sebald, S. Pruvost, D. Guyomar, Energy harvesting based on Ericsson pyroelectric cycles in a relaxor ferroelectric ceramic. Smart Materials and Structures. Vol. 17, pg. 15012 (2007). doi:10.1088/0964-1726/17/01/015012.

9 S. Pandya, G. Verlade, L. Zhang, J. D. Wilbur, A. Smith, B. Hanrahan, C. Dames, L. W. Martin, New approach to waste-heat energy harvesting: pyroelectric energy conversion. NPG Asia Materials. Vol. 11, pg. 26 (2019). doi:10.1038/s41427-019-0125-y.

10 K. Zhang, Y. Wang, Z. Wang, Y. Yang, Standard and figure-of-merit for quantifying the performance of pyroelectric nanogenerators. Nano Energy. Vol. 55, pg. 534–540 (2019). doi:10.1016/j.nanoen.2018.11.020.

11 N. Ma, K. Zhang, Y. Yang, Photovoltaic–pyroelectric coupled effect induced electricity for self-powered photodetector system. Advanced Materials. Vol. 29, pg. 1703694 (2017). doi:10.1002/adma.201703694.

12 P. Lheritier, A. Torelló, T. Usui, Y. Nouchokgwe, A. Aravindhan, J. Li, U. Prah, V. Kovacova, O. Bouton, S. Hirose, E. Defay, Large harvested energy with non-linear pyroelectric modules. Nature. Vol. 609, pg. 718–721 (2022). doi:10.1038/s41586-022-05069-2.

13 S. Pandya, J. Wilbur, J. Kim, R. Gao, A. Dasgupta, C. Dames, L. W. Martin, Pyroelectric energy conversion with large energy and power density in relaxor ferroelectric thin films. Nature Materials. Vol. 17, pg. 432–438 (2018). doi:10.1038/s41563-018-0059-8.

14 A. Sultana, M. M. Alam, T. R. Middya, D. Mandal, A pyroelectric generator as a self-powered temperature sensor for sustainable thermal energy harvesting from waste heat and human body heat. Applied Energy. Vol. 221, pg. 299–307 (2018). doi:10.1016/j.apenergy.2018.04.003.

15 Y. Tang, H. Luo, Investigation of the electrical properties of $(1\text{-}x)Pb(Mg_{1/3}Nb_{2/3})O_3\text{-}xPbTiO_3$ single crystals with special reference to pyroelectric detection. Journal of Physics D: Applied Physics. Vol. 42, pg. 075406 (2009). doi:10.1088/0022-3727/42/7/075406.

16 L. Liu, X. Wu, S. Wang, W. Di, D. Lin, X. Zhao, H. Luo, Growth and pyroelectric properties of rhombohedral $0.21Pb(In_{1/2}Nb_{1/2})O_3–0.49Pb(Mg_{1/3}Nb_{2/3})O_3–0.3PbTiO_3$ ternary single crystals. Journal of Crystal Growth. Vol. 318, pg. 856–859 (2011). doi:10.1016/j.jcrysgro.2010.11.033.

17 L. Li, X. Zhao, X. Li, B. Ren, Q. Xu, Z. Liang, W. Di, L. Yang, H. Luo, X. Shao, J. Fang, N. Neumann, J. Jiao, Scale effects of low-dimensional relaxor ferroelectric single crystals and their application in novel pyroelectric infrared detectors. Advanced Materials. Vol. 26, pg. 2580–2585 (2014). doi:10.1002/adma.201304546.

18 Q. Du, Y. Tang, X. Huang, F. Wang, X. Zhao, Z. Duan, X. Zhuang, W. Shi, J. Zhao, F. Liu, H. Luo, Structures and pyroelectric properties for [111]-oriented Mn-doped rhombohedral 0.36PIN-0.36PMN-0.28PT crystal. Journal of the American Ceramic Society. Vol. 102, pg. 7329–7335 (2019). doi:10.1111/jace.16600.

19 Y. Li, Y. Tang, J. Chen, X. Zhao, L. Yang, F. Wang, Z. Zeng, H. Luo, Enhanced pyroelectric properties and thermal stability of Mn-doped $0.29Pb(In_{1/2}Nb_{1/2})O_3\text{-}0.29Pb(Mg_{1/3}Nb_{2/3})O_3–0.42PbTiO_3$ single crystals. Applied Physics Letters. Vol. 112, pg. 172901 (2018). doi:10.1063/1.5024286.

20 H. Luo, G. Xu, H. Xu, P. Wang, Z. Yin, Compositional homogeneity and electrical properties of lead magnesium niobate titanate single crystals grown by a modified Bridgman technique. Japanese Journal of Applied Physics. Vol. 39, pg. 5581–5585 (2000). doi:10.1143/JJAP.39.5581.

21 C. Luo, C. Qiu, Y. Li, M. Wang, Y. Quan, Z. Xu, The effect of machining-generated residual stress on the properties of single crystal piezoelectric layers in high-frequency ultrasonic transducers. Journal of Materials Chemistry C. Vol. 13, pg. 9483–9493 (2025). doi:10.1039/d5tc00779h.

22 M. E. Lines, A. M. Glass, Principles and Applications of Ferroelectrics and Related Materials. Oxford University Press. pg. 141–148 (2001).

23 Y. Tang, H. Luo, X. Zhao, H. Xu, T. He, D. Lin, W. Jin, Structural quality of relaxor-based ferroelectric [111] oriented $Pb(Mg_{1/3}Nb_{2/3})O_3\text{-}PbTiO_3$ single crystals. Materials Science and Engineering: B. Vol. 134, pg. 32–35 (2006). doi:10.1016/j.mseb.2006.06.055.

24 T. Baba, Analysis of one-dimensional heat diffusion after light pulse heating by the response function method. Japanese Journal of Applied Physics. Vol. 48, pg. 05EB04 (2009). doi:10.1143/JJAP.48.05EB04.

25 I. M. McKinley, L. Pilon, Phase transitions and thermal expansion in pyroelectric energy conversion. Applied Physics Letters. Vol. 102, pg. 023906 (2013). doi:10.1063/1.4776668.

26 R. W. Whatmore, A. Patel, N. M. Shorrocks, F. W. Ainger, Ferroelectric materials for thermal IR sensors state-of-the-art and perspectives. Ferroelectrics. Vol. 104, pg. 269–283 (1990). doi:10.1080/00150199008223829.

27 Q. Li, S. Li, D. Pisignano, L. Persano, Y. Yang, Y. Su, On the evaluation of output voltages for quantifying the performance of pyroelectric energy harvesters. Nano Energy. Vol. 86, pg. 106045 (2021). doi:10.1016/j.nanoen.2021.106045.